Novel catalyst materials for the cathode side of MEAs suitable for transportation applications				
G.A. 303492				05.07.2016
Deliverable **D4.3**	WP4	**Electrochemical characterization of catalyst materials and selected catalyst/support combinations and study of chemical/morphological changes after the electrochemical workload**		
Deliverable: Publication on Pt_5Gd and Pt_3Y on standard carbon supports				
Description of Deliverable: Publication of results of electrochemical measurements on these alloys				
PM for D4.3: 1	Nature: R	Dissemination Level: PU	Delivery Date: 31.12.2014	Lead Beneficiary: DTU

Objectives of Work

- Ex-situ ORR activity measurements for novel electrocatalysts based on NPs from WP 3, Task 3.2 and 3.3, supported on standard carbon black;

Relevant Sections from the Description of Work

"Task 4.3: Electrochemical characterization of Pt_5Gd and Pt_3Y catalysts (month 9-30) (TUM, UniPd, DTU-CINF, CUT)

A further step ahead will be done applying the tools tested in task 4.2 to NPs of Pt_5Gd and Pt_3Y catalysts. This is an intermediate step before the new catalysts suggested by the WP2 will be available (see task 4.5). The Pt_5Gd and Pt_3Y will first be tested on standard carbon supports. In addition on selected samples the INPS method mentioned above will be applied in order to determine directly the catalysts state and other properties like catalyst dispersion during the electrochemical reaction. Experiments will include durability studies especially with respect to substrate corrosion, NP de-alloying and NP sintering. These will be done both by continuous operation at high current densities as well as under load change conditions. In the second part of this task, also advanced supports will be tested."

Description of Work Done / Results

The work done has been described in recent progress reports, and will be more detailed in the further deliverables of WP4, especially D4.5. Originally, TUM was the leading beneficiary of D4.3. However, as there has been no publication yet from TUM regarding the electrochemical performance of such alloy nanoparticles, instead the publication from DTU is cited here. In slight deviation from the description of work, this publication did not study the nanoparticles on Vulcan, but instead on glassy carbon.

Publication

A. Velázquez-Palenzuela, F. Masini, A.F. Pedersen, M. Escudero-Escribano, D. Deiana, P. Malacrida, T.W. Hansen, D. Friebel, A. Nilsson, I.E.L. Stephens, I. Chorkendorff, *The enhanced activity of mass-selected Pt_xGd nanoparticles for oxygen electroreduction*, Journal of Catalysis, 328 (2015) 297-307. The paper is attached to this deliverable, but is not open access.

Journal of Catalysis 328 (2015) 297–307

Contents lists available at ScienceDirect

Journal of Catalysis

journal homepage: www.elsevier.com/locate/jcat

The enhanced activity of mass-selected Pt_xGd nanoparticles for oxygen electroreduction

Amado Velázquez-Palenzuela [a], Federico Masini [a], Anders F. Pedersen [a], María Escudero-Escribano [a], Davide Deiana [b], Paolo Malacrida [a], Thomas W. Hansen [b], Daniel Friebel [c], Anders Nilsson [c], Ifan E.L. Stephens [a], Ib Chorkendorff [a,*]

[a] Center for Individual Nanoparticle Functionality (CINF), Department of Physics, Technical University of Denmark, Kongens Lyngby DK-2800, Denmark
[b] Center for Electron Nanoscopy (CEN), Technical University of Denmark, Kongens Lyngby DK-2800, Denmark
[c] SLAC National Accelerator Laboratory, 2575 Sand Hill Road, MS31, Menlo Park, CA 94025, USA

ARTICLE INFO

Article history:
Received 24 September 2014
Revised 31 October 2014
Accepted 9 December 2014

This research article is dedicated to the memory of Haldor Topsøe (1913–2013), who was always a strong proponent of fundamental research toward improved catalysis.

Keywords:
Electrocatalysis
Fuel cells
Oxygen reduction reaction
Nanoparticles
Platinum–gadolinium alloy
Core/shell
Strain effect

ABSTRACT

Mass-selected platinum–gadolinium alloy nanoparticles (Pt_xGd NPs) are synthesized for the first time as oxygen reduction reaction (ORR) electrocatalysts using the gas aggregation technique, under ultrahigh vacuum (UHV) conditions. The morphology of the Pt_xGd catalysts is characterized, and their catalytic performance toward the ORR is assessed in acidic media using a half-cell configuration. The Pt_xGd 8-nm catalyst shows a high activity (3.6 A $(mg\ Pt)^{-1}$), surpassing the highest activity reached so far with Pt_xY NP catalysts. In addition, the optimum Pt_xGd catalyst also presents high stability, as suggested by the accelerated stability tests under ORR potential cycling. Extended X-ray absorption fine structure (EXAFS) spectroscopy measurements confirm that as-prepared Pt_xGd NPs are compressively strained, relative to pure Pt, and that a Pt_xGd core/Pt-rich shell structure is adopted after partial Gd leaching. The activity correlates strongly with the compressive strain. On that basis, we propose that the ORR enhancement is due to the compressive strain within the Pt shell induced by the alloy core. The results herein confirm the suitability of Pt_xGd NPs as cathode nanocatalysts for proton exchange membrane fuel cells (PEMFCs).
© 2014 Elsevier Inc. All rights reserved.

1. Introduction

Both electrocatalysis and traditional heterogeneous catalysis focus on surface reactions that involve multistep reaction pathways, with sequential breaking and/or creation of chemical bonds. The catalyst consists of supported nanoparticles whose atomic and electronic structures are analyzed by means of common characterization techniques, such as X-ray photoelectron spectroscopy (XPS), transmission electron microscopy (TEM), or X-ray absorption spectroscopy (XAS) [1]. The main difference between the fields is that in electrocatalysis, the structure of the electrified metal/solution interface needs to be taken into account, which contains solvent molecules and other charged species. Despite these inherent challenges, it turns out that the factors that control the reactivity of surfaces toward gas/solid catalytic reactions are largely the same as for electrocatalytic reactions, that is the binding to the reaction intermediates [2]. Sabatier's principle states that the optimum catalyst should bind neither too weakly nor too strongly to the reaction intermediates [3]. According to the density functional theory (DFT) calculations of Nørskov, Rossmeisl and coworkers, the binding energies of the reaction intermediates in multielectron reactions tend to scale linearly together [4,5]. Consequently, the binding energy of just one reaction intermediate can be used as descriptor to predict the trends in activity for electrocatalytic reactions; plotting the activity as a function of such a descriptor then results in a Sabatier volcano. This model has been able to describe trends for a number of electrocatalytic reactions [6–15], in particular the oxygen reduction reaction (ORR) [4,13,16–22]. It turns out that proton exchange membrane fuel cells (PEMFCs) are limited by the ORR. Consequently, large loadings of Pt nanoparticle catalysts are required at the cathode to limit potential losses, as Pt is the most active pure metal catalyst for the reaction [23]. Typically, the Pt loading at the PEMFC cathode, where the ORR takes place,

* Corresponding author.

http://dx.doi.org/10.1016/j.jcat.2014.12.012
0021-9517/© 2014 Elsevier Inc. All rights reserved.

is around one order of magnitude higher than the Pt loading at the anode (0.4 mg Pt cm^{-2} versus 0.05 mg Pt cm^{-2}) where the hydrogen oxidation reaction (HOR), which is far more facile, occurs [23–27]. As a result, the high cost and short supply of Pt hinder the large-scale uptake of PEMFCs, despite their promise as efficient, potentially zero-emission source of power for automotive vehicles and portable devices [28].

A suitable strategy in order to improve the ORR activity, and hence, reduce the Pt loading at the cathode, is to use Pt alloys instead of pure Pt [16,23,28–30]. The effect of alloying is to weaken the binding of the surface to the hydroxyl intermediates. In accordance with the volcano model [4], the overpotential on pure Pt catalysts is due to the reduction of *OH (where *OH is an adsorbed hydroxyl intermediate) [4,16,31–34]. The optimum catalyst for the ORR should have an *OH binding energy 0.1 eV weaker than Pt(1 1 1), or an O* binding 0.2 eV weaker; excessive weakening of HO* will cause the reaction to be limited by the formation of the superhydroxyl intermediate, HOO* [35]. Typically, the surface atoms of a Pt alloy will consist of pure Pt, as most other metals will be unstable at the oxidizing, acidic, conditions of a PEMFC cathode. Thereby, the introduction of a second metal in the Pt structure induces a change in the electronic structure of the Pt surface atoms; this can either be induced because of direct interactions with the second metal, that is the *ligand effect* [19,36,37] and/or the existence of lattice compression (*strain effect*), as a result of a decrease of the Pt–Pt interatomic distances [38–40].

In recent years, efforts have been focused on Pt alloys with late transition metals (LTM), such as Fe, Ni, Cu, and Co; they have shown considerably greater activity compared to pure Pt [41–51]. The active phase in these alloys is a Pt overlayer whose thickness strongly depends on the catalyst pre-treatment [46]. Thus, the Pt overlayer is typically one monolayer thick when the Pt–LTM alloy is subjected to annealing in ultrahigh vacuum (UHV) conditions prior to the electrochemical characterization (“Pt-skin” surface) [46]. In contrast, a considerably thicker, ~1-nm Pt overlayer, equivalent to 3–4 monoatomic Pt layers, is achieved when the alloy is exposed to the acidic electrolyte, because of leaching of the less noble metal from the outermost atomic layers of the surface (denoted by Markovic, Stamenkovic and coworkers as a “Pt-skeleton” surface) [46,52]. On such a thick Pt overlayer, ligand effects can be excluded, and hence, the ORR enhancement should be due to surface strain effects.

Although these Pt alloy catalysts show significant initial enhancements in activity, relative to pure Pt, over time their performance tends to degrade: the second element will segregate to the surface and dissolve into the electrolyte, via a process known as dealloying [43,48,53–58].

As a result of the instability of alloys of Pt and late transition metals, we, in collaboration with theory group of Nørskov and Rossmeisl, screened for a more stable class of Pt alloy ORR catalysts, using computational DFT-based screening methods [18]. We searched for alloys that were not only predicted to be active, on the basis of the O* binding, but also stable, as predicted by the alloying energy; the output of the screening was that both Pt_3Y and Pt_3Sc should be active and stable. Subsequent experiments on sputter-cleaned polycrystalline Pt_3Y showed that it exhibited exceptionally high activity for the ORR, only surpassed by single crystal Pt_3Ni(1 1 1) with an annealed “Pt-skin” structure [50]. The considerable negative alloying energy (or heats of formation) of Pt_3Y and Pt_3Sc ($\Delta H_{f(alloy)} \approx -4$ eV/formula unit) is also shared by other Pt alloys with early transition metals and lanthanides, such as Pt_5La, Pt_5Ce, and Pt_5Gd; this contrasts with the negligible heat of formation of the Pt–LTM intermetallic compounds (LTM = Fe, Co, Cu, Ni; $\Delta H_{f(alloy)} > -1$ eV) [59,60] (we note that despite their denomination as “rare earths,” the lanthanide metals are much more abundant and more inexpensive than Pt [61]). We are aware that despite the significant heat of formation of the Pt–lanthanides alloys, there is still an immense driving force for the dealloying of the solute metal under the corrosive environment of a PEMFC cathode. Nevertheless, we expect that the dealloying mechanism ultimately involves an energy barrier for diffusion determined at least partially driven by the heat of formation of the bulk alloy, hence its use as a descriptor of the kinetic stability [18]. This notion is consistent with surface science experiments performed at our laboratory: a Cu monolayer on Pt(1 1 1) will diffuse subsurface at ~500 K [62]; under the same conditions, an Y monolayer on Pt(1 1 1) will diffuse subsurface at ~800 K [63]. This is likely due to the stronger interaction between Pt and Y than between Pt and Cu, ($\Delta H_{f(Pt3Y)} \approx -4.04$ eV/formula unit than $\Delta H_{f(Pt3Cu)} \approx -0.56$ eV/formula unit) [18]. On the other hand, adsorbed O* or subsurface oxide may induce the segregation of the solute element [64], but only when the oxygen atom is in close vicinity to the solute metal.

Our subsequent electrochemical experiments also revealed that other Pt–lanthanide alloys show superior activity for the ORR in the bulk polycrystalline form, in particular Pt_5Gd, which shows a similar activity to Pt_3Y [30,59,60,65]. We must emphasize that sputter-cleaned polycrystalline Pt_5Gd and Pt_3Y alloys have displayed the highest ORR activities ever reported in the literature, to the best of our knowledge the highest for samples prepared in this manner (fivefold increase at 0.9 V, compared to polycrystalline Pt) [60,65]. Furthermore, these intermetallic compounds exhibit a high stability under ORR conditions. For example, Pt_5Gd only exhibits 15% activity loss after 10,000 cycles between 0.6 and 1.0 V in O_2-saturated electrolyte [59,60]. In comparison, Todoroki and coworkers demonstrated that Pt-enriched Ni/Pt(1 1 1) lost 75% of its initial activity under similar experimental conditions [48]. Moreover, the great stability of Pt–early transition metal alloys has been also confirmed by Lim and co-workers through analysis of sputtered thin-film electrodes [66].

It turns out that the origin of activity of Pt_3Y was somewhat more complicated than we originally anticipated [63,65]. Angle-resolved X-ray photoelectron spectroscopy (AR-XPS) analysis of the sputter-cleaned alloyed electrodes showed that a Pt-skeleton structure is developed after the electrochemical experiment, the Pt overlayer being around 1 nm thick. A similar structure was also found for Pt_5Gd alloy after the electrochemical measurement [60], and, consequently, the ORR enhancement in both cases was attributed to compressive strain imposed onto the Pt overlayer by the alloy bulk. Such behavior seems counterintuitive, given that Y and Gd have a larger covalent radius than Pt [67]; one could expect that the resulting alloy would induce surface tensile strain, leading to a stronger adsorption of *OH and a higher overpotential for the ORR. Nevertheless, we explain the superior ORR activity of Pt_xY and Pt_5Gd compared to pure Pt by considering the inherent structural characteristics of such alloys. In order to accommodate the different Pt and second metal atomic radii, most of the Pt atoms are arranged in *kagomé* nets with a very short Pt–Pt nearest-neighbor distance (<2.7 Å) and with larger voids in which the solute atoms reside with bond lengths greater than 3 Å to their neighbor atoms (see Fig. S1 in the Supplementary information for an illustrative example of such arrangement). On the basis of the described structure, we proposed that Pt_xY and Pt_5Gd alloys impose compressive strain onto the Pt overlayer [60,65], resulting in weaker *OH adsorption and enhanced oxygen reduction activity.

In light of our results with extended surfaces of Pt_xY and Pt_xGd, we aimed to synthesize the catalysts in the more technologically relevant nanoparticulate form. Nevertheless, this task is not trivial, because of the difficulties of synthesizing the non-noble metal in the metallic state, due to the particularly negative standard reduction potential of Gd or Y ($U^0(Gd^{3+}/Gd) = -2.28$ V and $U^0(Y^{3+}/Y) = -2.37$ V); in comparison, late transition metals, such as Ni, have

a much more positive dissolution potential ($U^0(Ni^{2+}/Ni) = -0.25$ V) [68]. This drawback makes it highly challenging to synthesize Pt_xGd and Pt_xY alloy nanoparticles by means of traditional wet chemical methods, which would involve the exposure of the non-noble metal to oxygen or water [69]. Consequently, in order to prove that nanoparticles of this class of catalysts could be worthy of further investigation, and eventual chemical synthesis, we resorted to a physical method for producing Pt_xY nanoparticles [70]. Our chosen route was the gas aggregation method, combined with time-of-flight separation after sputtering of a primary alloy target [70–75]. Apart from providing a proof-of-concept, this method also produces catalysts with a well-defined size, shape, morphology, and composition, providing significant scientific insight. The corresponding ORR activities displayed in the electrochemical experiments avoid typical secondary factors, such as possible interactions of the nanoparticles with a high surface area carbon substrate or the influence of the metal precursors/solvents employed in the synthesis [76–80]. Our work showed that the ORR activity of Pt_xY nanoparticles supported on a planar glassy carbon support showed a marked size dependence; the 9-nm catalyst showing an exceptionally high mass activity of 3.05 A $(mg\ Pt)^{-1}$ only surpassed by the performance of annealed Pt_3Ni nanoframes [41]. In addition, the Pt_xY catalyst retained 63% of the activity after accomplishing the long-term stability test under ORR conditions. These results confirmed that the high ORR activity of the sputter-cleaned Pt_3Y alloy [18] could be extended to the nanoparticulate form and that they show moderate stability.

Herein, we extend this approach to perform structural and electrochemical characterization of Pt_xGd alloy nanoparticles synthesized by the gas aggregation method, following the same procedure used for the production of Pt_xY nanoparticles. The activity of the Pt_xGd nanoparticles toward the ORR was evaluated in half-cell configuration by using the rotating ring-disk electrode (RRDE) technique. In addition, the composition and morphology changes of the catalysts before and after the electrochemical test were characterized by means of XPS, transmission electron microscopy (TEM), and extended X-ray absorption fine structure (EXAFS) spectroscopy measurements.

2. Materials and methods

2.1. Synthesis of mass-selected Pt_xGd nanoparticles

The nanoparticles were prepared using a magnetron sputter gas aggregation source (Birmingham Instruments Inc.), combined with time-of-flight mass filtering, and deposited onto glassy carbon electrodes mounted in an multichamber ultrahigh vacuum (UHV) system (Omicron, Multiscan Lab) with a base pressure in the 10^{-11} mbar region. The gas aggregation technique involves Ar^+ sputtering of an alloy target (in this study a Pt 9:1 Gd alloy target from Kurt J. Lesker Inc.), to produce an atomic vapor that is condensed into nanoparticles through collisions with cooled Ar and He gas. It must be noted that the composition of the target determines the atomic ratio of the mass-selected nanoparticles, as demonstrated with Pt_xY nanoparticles in our preceding publications [70,81]. It turns out the use of a target with the same composition than the corresponding extended, polycrystalline alloy of interest leads to nanoparticles with high solute content that would corrode in excess [65,70,81]. Consequently, in the present study, we used the same 9:1 ratio for the synthesis of Pt-rich Pt_xGd nanocatalysts.

The gas aggregation method is particularly useful in the context of metallic formation of nanoparticles from metals such as gadolinium that has high affinities for oxygen, as it is an ultrahigh vacuum compatible method: oxygen is present in extremely low levels and therefore it can entirely be avoided in the as-deposited Pt–Gd alloy particles. The second major advantage arises from the fact that many of the nanoparticles produced via aggregation of Ar^+ sputtering atoms are ionized [82]; thus, the particles can be filtered based on their mass-to-charge ratio, which in turn allows the deposition of particles with narrow size distributions. In our experiments, the Pt–Gd nanoparticles are filtered using a time-of-flight mass filter [83].

Following the particle production and filtering stages, the ionized nanoparticles were directed using Einzel lenses onto glassy carbon electrode supports mounted in the vacuum chamber. The Einzel lenses can be used to control the breadth and position of the particle beam, which gives control of the total number of particles that are deposited onto the electrode surface, as well as the density of the nanoparticles. The combination of particle counting and mass selection allows us to accurately estimate the amount of catalyst deposited onto the glassy carbon substrate. The mass that was used for the calculation of the mass activity was the mass calculated from the deposition current.

Assuming spherical and singly charged particles, the total deposited mass was calculated from the formula $M_{dep} = m_p I_{dep} t$, where m_p is the single particle mass, set using the mass filter, I_{dep} the deposition current and t the deposition time. This mass, from the deposition current, combined with the Pt:Gd ratio estimated from the XPS measurements of the as-prepared catalysts, was used to determine the mass activity for the ORR.

Elemental characterization of the as-prepared glassy carbon-supported Pt–Gd nanoparticles was performed in-situ for each nanoparticles size, that is without breaking the vacuum, using X-ray photoelectron spectroscopy (XPS). The X-ray source was an XR-50 from Specs GmbH., with aluminum and magnesium anodes. XPS and ISS measurements after air exposure and after electrochemical testing were conducted in a different UHV system.

2.2. X-ray photoelectron spectroscopy (XPS)

X-ray photoelectron spectroscopy (XPS) measurements were acquired in two different UHV chambers. A preliminary analysis of the as-prepared nanoparticles was performed in-situ, soon after deposition. In this first experimental setup, the X-ray source (XR-50 manufactured by SPECS GmbH) consisted of Mg anode (Mg Kα emission line at 1253.6 eV). The XPS spectra were measured with an Omicron hemispherical analyzer with a pass energy of 25 eV. Ex-situ measurements of the samples after air exposure, after ORR activity tests, and after stability tests were instead performed in a Theta-Probe instrument (Thermo Scientific). This instrument is equipped with a monochromatized Al Kα source (emission line at 1486.7 eV), and XPS spectra were obtained at an analyzer pass energy of 100 eV. In all cases, the atomic concentrations were quantified by integration of the Pt 4f, Gd 4d, O 1s, C 1s peaks after removal of a Shirley-type background. The resulting XPS intensities were corrected for the transmission function of the analyzers, Wagner sensitivity factors [84], and electron mean free path estimated from the TPP-2M formula [85].

2.3. Transmission electron microscopy (TEM) analysis

Bright-field transmission electron microscopy (TEM) and high-angle annular dark-field scanning transmission electron microscopy (HAADF-STEM) were performed in a FEI Titan Analytical 80-300 equipped with a CEOS C_s probe aberration corrector on the condenser lens. Identical location (IL) studies were carried out in bright-field TEM at 300 kV accelerating voltage. The particle size distributions (PSDs) were extracted from HAADF-STEM micrographs acquired at 300 kV accelerating voltage. Within each specimen, the HAADF-STEM images were analyzed with the same microscope condition, constant acquisition dwell time as well as

the HAADF detector settings. For the TEM measurements, the nanoparticles were deposited directly onto lacey carbon-coated Au TEM grids. The setup for the electrochemical stability test under ORR conditions was adapted from the procedure developed from an earlier study at our laboratory [86].

2.4. Electrochemical measurements

The electrochemical testing of the Pt_xGd nanoparticles was carried out in a custom-made three-electrode glass cell provided with an external jacket attached to a water bath with temperature control. The counter electrode was a Pt wire, and the reference was a $Hg|Hg_2SO_4$ electrode, both separated from the working electrode compartment using ceramic frits. The electrolyte, 0.1 M $HClO_4$, was prepared using high-purity 70% $HClO_4$ (Merck, Suprapur) and ultrapure water (Millipore Milli-Q, resistivity >18.2 MΩ cm^{-1}), whereas all the gases used in the electrochemical tests were grade 5N5 (AGA). All the measurements were accomplished at 23 ± 1 °C.

The electrochemical experiments were performed with a VMP2 multi-channel potentiostat (Bio-Logic Instruments) computer controlled using EC-Lab software. The rotating ring-disk electrode (RRDE) assemblies and the glassy carbon (GC) substrates (5 mm diameter) were acquired from Pine Instruments Corporations and HTW, respectively. All the potentials indicated in the text are referred to the reversible hydrogen electrode (RHE) measured in the same electrolyte and corrected for Ohmic losses.

In each experiment, the GC disk containing the as-prepared Pt_x-Gd nanoparticles was inserted into a RRDE Teflon holder and used as working electrode for the electrochemical test. Subsequently, the electrode was immersed into the electrochemical cell under potential control at 0.10 V in N_2-saturated 0.1 M $HClO_4$ electrolyte and subjected to potential cycling between 0.05 V and 1.00 V at 50 mV s^{-1} until a stable cyclic voltammogram was achieved. Following this, the ORR performance of the Pt_xGd nanoparticles was evaluated by means of hydrodynamic voltammetry in O_2-saturated solution. After the ORR experiment, CO-stripping analysis was carried out for determining the electrochemical surface area (ECSA) of the Pt_xGd nanoparticles. For this purpose, CO gas was first bubbled into the electrolyte for 2 min, while the working electrode potential was kept at 0.05 V; then, the remaining CO dissolved in solution was removed by sparging Ar for 15 min whereas keeping the potential control. Afterward, the potential was scanned up to 1.00 V in CO-free Ar-purged solution at 50 mV s^{-1}. The corresponding electrochemical active surface area (ECSA) of the Pt_xGd catalysts was estimated assuming a ratio of 420 μC cm^{-2} [87].

The long-term stability of the Pt_xGd nanoparticles was subjected to analysis by cycling between 0.60 and 1.00 V at 100 mV s^{-1} in quiescent O_2-saturated 0.1 M $HClO_4$ solution for a total of 10,000 potential cycles. The ORR activity was evaluated after 1000 and 10,000 potential cycles. A second CO-stripping experiment was performed in order to probe the possible change of the electrochemical area after the stability test.

2.5. Extended X-ray absorption fine structure (EXAFS) analysis

Grazing incidence X-ray absorption spectroscopy (GI-XAS) measurements were carried out at beam line 11-2 at the Stanford Synchrotron Radiation Lightsource (SSRL). An absorption spectrum around the Pt L_3 edge (11,564 eV) was acquired for each sample, and the energy range was 11,334–12,273 eV, which corresponds to an EXAFS range up to a photoelectron wave number of 13.6 $Å^{-1}$. The samples were aligned in grazing incidence geometry near the critical angle of total external reflection in order to maximize the fluorescence yield. The fluorescence photons from the Pt atoms in the nanoparticles were captured using a 100-element Ge solid-state detector. Several spectra were recorded for each sample and subsequently averaged to increase the signal-to-noise ratio. The data analysis was done using the program SixPACK, which is based on the IFEFFIT program. EXAFS fitting was done in *R*-space using a *k*-weighting of k^2, a *k*-range of 3–11 $Å^{-1}$, and an *R*-range of around 1.5–3.2 Å. A detailed description of the data treatment and the fitting procedure can be found in the Supplementary information.

3. Results

3.1. Synthesis of mass-selected Pt_xGd nanoparticles

The mass-selected Pt_xGd particles were prepared through combination of gas aggregation of a Pt_9Gd target and time-of-flight separation as shown in Fig. 1. The charged nanoparticles were subsequently deposited directly onto a planar glassy carbon substrate under ultrahigh vacuum conditions. In order to define the overall particle composition, XPS measurements were acquired in-situ after deposition. Fig. S2 shows that the Pt:Gd ratios were rather similar in all cases, irrespective of the particle size, with an average value of 3.6 ± 0.8.

3.2. X-ray photoelectron spectroscopy (XPS)

Further XPS characterization was carried out ex-situ after exposure of the samples to air and after electrochemical ORR activity testing. Fig. 2 reports the XPS spectra of the Gd 4d core-level region for a 9-nm sample in different conditions: very similar spectra

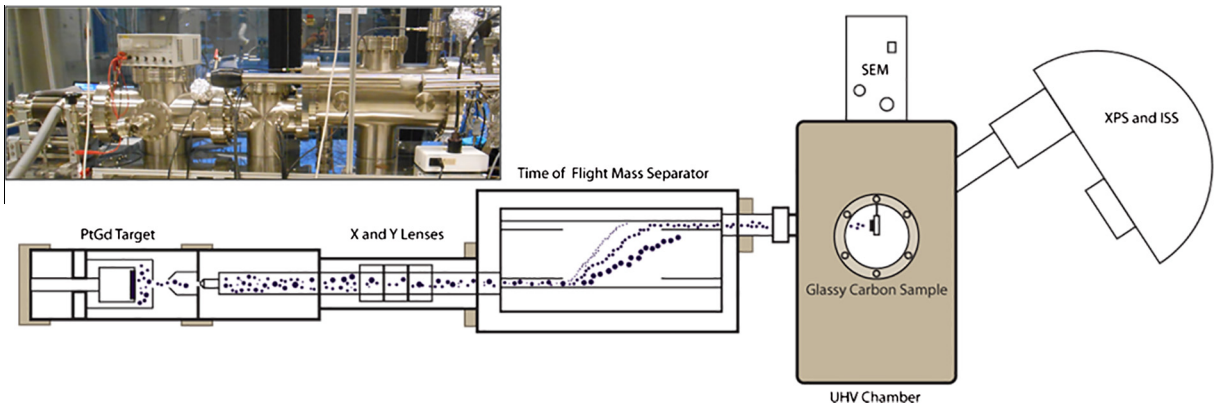

Fig. 1. Schematic representation of the nanoparticle source used for the synthesis and characterization of the Pt_xGd nanoparticles in UHV conditions. The inset shows a photograph of the actual apparatus.

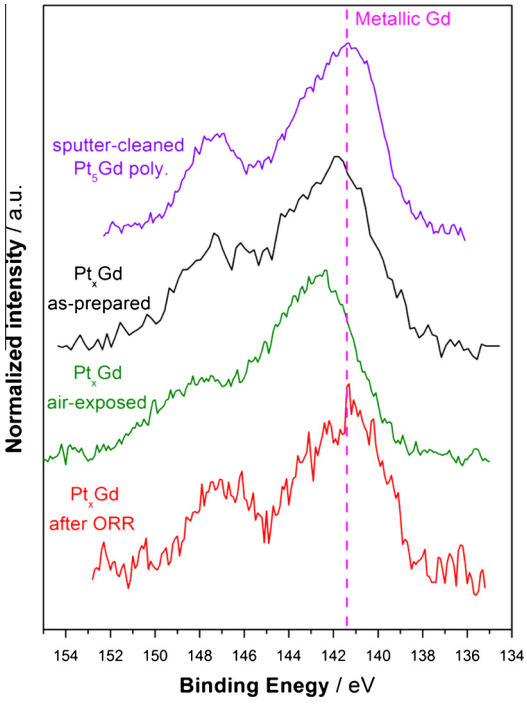

Fig. 2. Detailed XPS survey of Gd 4d core-level region spectra for sputter-cleaned polycrystalline Pt_5Gd and for the Pt_xGd nanoparticles (9 nm) as-prepared (under UHV conditions), after air exposure and after the ORR measurement.

were also taken for different particle sizes indicating that the following considerations can be extended to all Pt_xGd nanoparticles. As typical for the lanthanide metals, the XPS features of Gd are in general quite complex due to presence of localized electrons in the 4f shell. The localized f electrons couple through Russell–Saunders and spin–orbit coupling and result in a complex broad multiplet structure, see Fig. 2 [88]. In principle, this could be fitted using the multiplet structure, but we have here chosen to perform a careful analysis of the peak position and a comparison with the reference spectrum of a sputter-cleaned Pt_5Gd polycrystalline alloy where Gd atoms are in a completely metallic state allows us to monitor the chemical state of Gd. In the case of the as-deposited 9-nm Pt_xGd nanoparticles, the position of the Gd 4d spectrum is very similar to the polycrystalline sample, demonstrating that the synthesis of alloyed nanoparticles was successful and that no Gd oxidation occurred. However, as soon as the nanoparticles are taken out of the deposition chamber and exposed to air, a clear shift of the Gd 4d features and a change of shape can be observed and the new peak position agrees with the formation of Gd oxide on the surface [88]. Notably, these oxidized components are completely removed after electrochemical measurements, suggesting that the oxide is not stable in acid and dissolves in the electrolyte, in agreement with the Pourbaix diagram for Gd [68]. The remaining Gd signal resembles closely the as-prepared nanoparticles and that of clean polycrystalline Pt_5Gd; this indicates that a Pt overlayer is formed during the acid leaching of surface Gd and this Pt shell protects the alloyed Gd in the core from further oxidation or dissolution [60]. The formation of such core–shell structure is also supported by the measured Pt:Gd ratios in Fig. S2: for all particle sizes

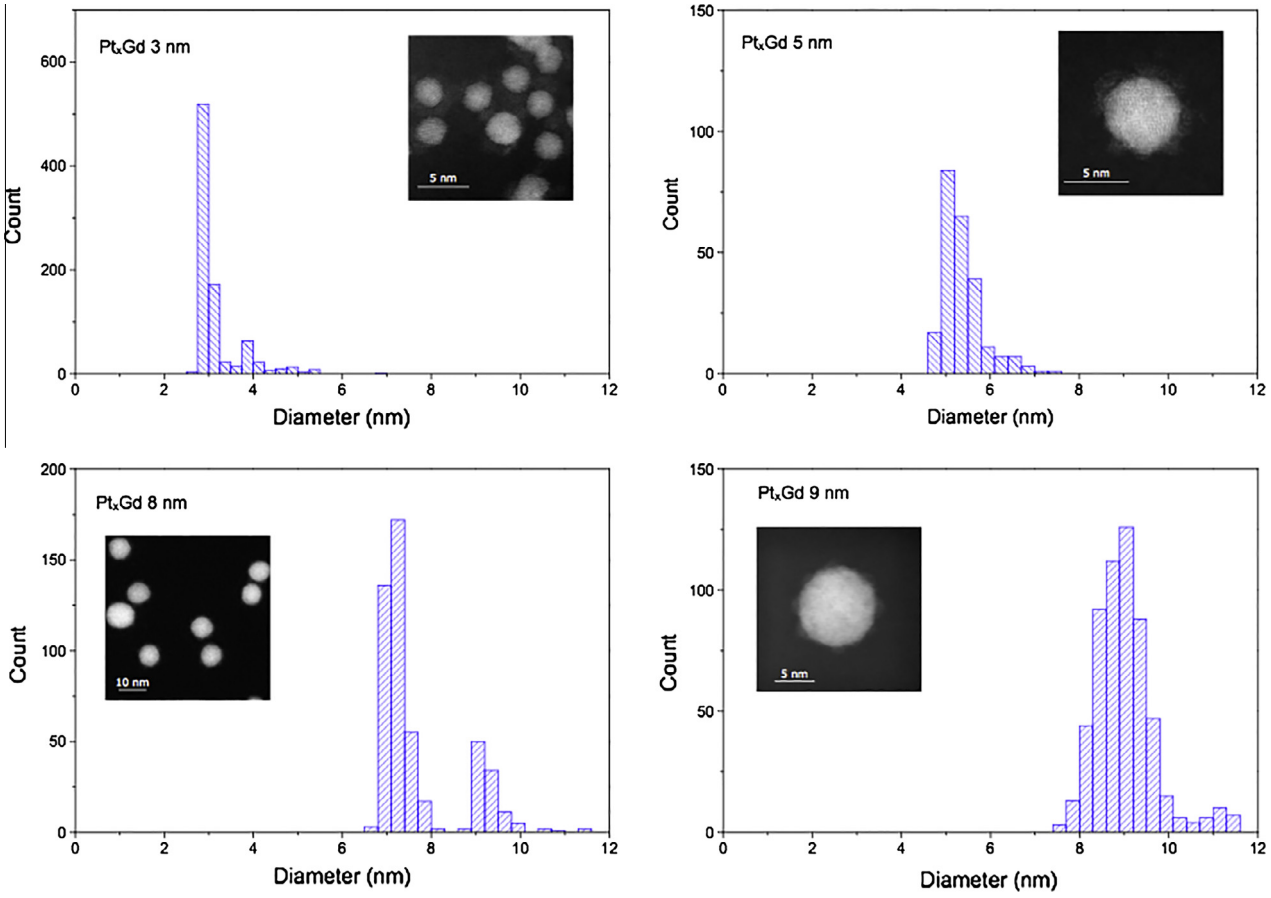

Fig. 3. Particle size distributions and representative HAADF-STEM micrographs of the different Pt_xGd nanoparticle catalysts.

and in particular for the small nanoparticles, the relative amount of Pt after electrochemistry is considerably higher than for the as-prepared or air-exposed nanoparticles. It should be noticed that analogous XPS evidences were found for Pt_xY nanoparticles in our previous study, supporting the notion that a similar core–shell structure is formed [70].

3.3. Transmission electron microscopy (TEM) analysis

Fig. 3 shows the particle size distribution (PSD) histograms of the different particles determined by HAAD-STEM. As seen, nanoparticulate catalysts with mean particle sizes ranging between ~3 and ~9 nm were synthesized. For simplicity, the particle sizes are rounded up to the closest integer to denominate the different catalysts; however, when plotting electrochemical or morphological parameters as a function of the size, the actual measured value and the corresponding standard deviation are employed, as indicated in Table S1 in the Supplementary information. The PSDs present narrow peaks at the selected sizes indicating the successful mass selection. The satellite peaks at higher diameters correspond to double-charge nanoparticles, with a mass twice the intended one. This undesired effect is minimized by optimizing the synthesis conditions, namely by stabilization of the deposition current during the nanoparticles deposition [81]. IL Bright-field TEM of the 8-nm sample is shown in Fig. 4. The images of the as-prepared Pt_x-Gd catalyst and the following stability test under ORR conditions indicate the high stability of the nanoparticles on the carbon film support. A closer inspection of the exact same nanoparticles at high magnification reveals an amorphous shell covering the particles on the untreated sample that disappears after ORR catalytic test. In light of the XPS results, the amorphous shell can be ascribed to an oxide formed during air exposure. Presumably, the oxide would be dissolved in the electrolyte in the early stages of the electrochemical experiments.

3.4. ORR measurements of Pt_xGd catalysts

Following the sample preparation and the preliminary morphological characterization, the alloyed nanoparticles supported on glassy carbon were electrochemically tested in 0.1 M $HClO_4$ using a rotating ring-disk assembly. As a first step, the catalysts were electrochemically activated by means of potential cycling between 0.05 V and 1.00 V in N_2-saturated electrolyte until a stable voltammogram was achieved, as indicated in Fig. S3 of the Supplementary information, and subsequently the ORR experiment was carried out in O_2-saturated electrolyte under hydrodynamic conditions. The activity of the Pt alloy catalysts at 0.9 V, expressed in terms of specific activity and mass activity (normalized by Pt loading), is presented in Fig. 5 as a function of the nanoparticle size. For comparison purposes, our previous results obtained with mass-selected Pt_xY and Pt nanoparticles are also included [70,71]. The activities of sputter-cleaned, polycrystalline Pt_5Gd and Pt_3Y extended surfaces, as well as sputter-cleaned, polycrystalline Pt are also presented in Fig. 5. The obtained size dependence of the specific activity for the Pt_xGd nanoparticles is in agreement with the trend found for both mass-selected Pt_xY and Pt nanoparticulate catalysts, namely the ORR-specific activity increases with the nanoparticle size, with the activity of the larger nanoparticles approaching the result reported for the corresponding extended, polycrystalline surface. From Fig. 5, it is manifest the superior activity of the Pt_xGd nanoparticles compared to pure Pt catalysts, with the only exception of the analyzed smallest size (3 nm),

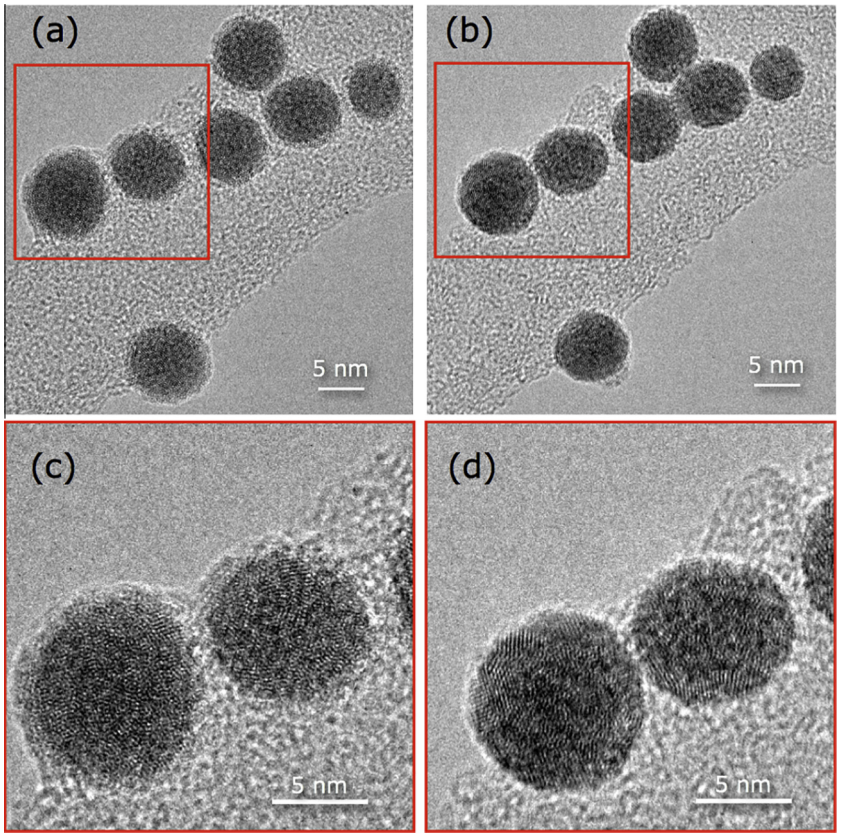

Fig. 4. Bright-field IL-TEM micrographs of 8-nm Pt_xGd nanoparticles before (a) and after (b) stability test. The (c and d) images are a magnification of the red squares drawn in (a and b), respectively. (For interpretation of the references to color in this figure legend, the reader is referred to the web version of this article.)

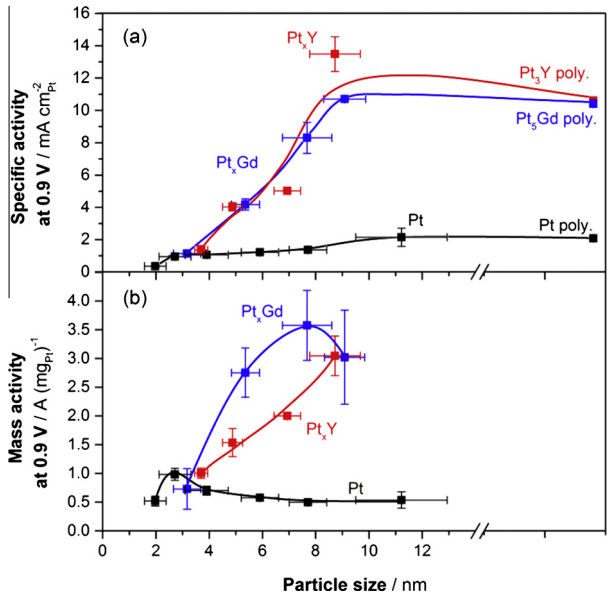

Fig. 5. (a) Specific activity and (b) mass activity of Pt_xGd nanoparticles (blue). Data taken at 0.9 V from cyclic voltammetry recorded at 50 mV s^{-1}, 1600 rpm, and 23 ± 1 °C in O_2-saturated 0.1 M $HClO_4$. For comparison, the previously published mass and specific activities of mass-selected Pt_xY (red) and pure Pt nanoparticles (black) are also plotted [70,71]. Additionally, the specific activities obtained under the same conditions of sputter-cleaned polycrystalline Pt_5Gd and Pt_3Y extended surface electrodes, as well as sputter-cleaned polycrystalline Pt, are presented [60]. Each data point corresponds to the mean value from at least two independent electrochemical tests. The horizontal error bars show the standard deviation in the particle size distribution (PSD) whereas the vertical error bars show the standard deviation in electrochemical measurements. The lines serve as a guide for the eye. The Supplementary information contains details of the quantification of mass and surface area carried out for the activity evaluation. (For interpretation of the references to color in this figure legend, the reader is referred to the web version of this article.)

similar to the performance achieved with the Pt_xY nanoparticles of a comparable particle size (4 nm) [70]. Additionally, the enhanced activity factor of the Pt_xGd catalysts is similar to that observed for Pt_xY nanoparticles, indicating that the equivalent promotional effect for the ORR found with Pt_3Y and Pt_5Gd bulk alloys is also attained in the nanoparticulate form. This is a subject of special interest regarding the potential application of Pt_xY and Pt_xGd electrocatalysts in PEMFC cathodes. Moreover, the specific activity of the 9-nm samples of each alloy (13.5 mA cm^{-2} and 10.7 mA cm^{-2} for Pt_xY and Pt_xGd, respectively) is comparable, or marginally higher, than that reported for carbon-supported annealed Pt_3Ni nanoframes (~20 nm), synthesized by Stamenkovic and co-workers (8.5 mA cm^{-2}) [41].

On the other hand, the mass activity evaluated as a function of the size reveals not only the greater mass activity of the Pt_xGd catalysts compared to pure Pt nanoparticles, but also the higher performance versus the Pt_xY catalysts. In the case of the Pt_xGd nanoparticles, the size dependence of the mass activity originates a volcano plot with the highest mass activity achieved with the 8 nm size and being equal to 3.6 A (mg Pt)$^{-1}$, which is significantly higher than the optimum mass activity reported for the Pt_xY nanoparticles in our previous work (3.0 A (mg Pt)$^{-1}$, with 9 nm as set particle size). Moreover, the maximum mass activity is ~3.6 times higher than the optimum result found with the pure Pt nanoparticles synthesized using the same size-selection experimental procedure [71] and roughly 6.5 times higher than the most active carbon-supported pure Pt electrocatalyst (0.55 A (mg Pt)$^{-1}$) [89]. The remarkable mass activity peak of the Pt_xGd nanoparticles also represents *the highest ORR activity reported in the literature for solid nanoparticles* (opposed to hollow or porous nanocatalysts) *based on an acid-leached structure*; it is only overtaken overall by the performance of Pt_3Ni nanoframes (5.7 A (mg Pt)$^{-1}$) [41].

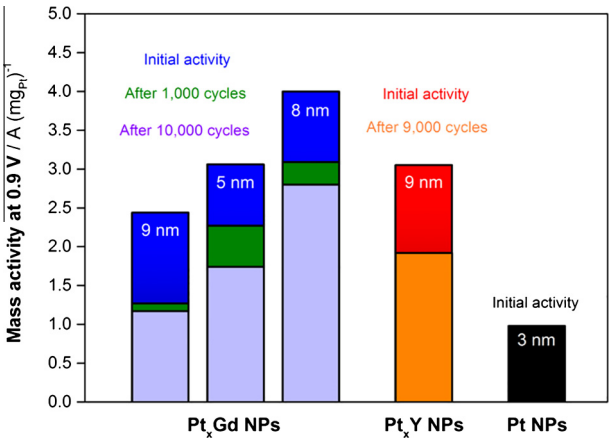

Fig. 6. The initial mass activity of Pt_xGd nanoparticles (blue), and after 1000 cycles (green) and 10,000 cycles (violet) of stability test under ORR conditions. The initial performance of the most active Pt_xY catalyst (red) and after 9000 cycles of stability test (orange) is also displayed [70]. For a suitable comparison, the maximum activity reported for mass-selected Pt NPs is also plotted (black) [71]. Data taken at 0.9 V from cyclic voltammetry recorded at 50 mV s^{-1}, 1600 rpm, and 23 ± 1 °C in O_2-saturated 0.1 M $HClO_4$. Stability test carried out by potential cycling between 0.6 and 1.0 V at 100 mV s^{-1}, 0 rpm, and 23 ± 1 °C in O_2-saturated 0.1 M $HClO_4$ solution. A detailed description of the stability test procedure is found in the Supporting information. (For interpretation of the references to color in this figure legend, the reader is referred to the web version of this article.)

In order to investigate the stability of the Pt_xGd nanoparticles, long-term potential cycling experiments under ORR conditions were carried out. For this purpose, the alloyed electrodes were cycled between 0.6 V and 1.0 V for 10,000 cycles in O_2-saturated 0.1 M $HClO_4$ [53,55]. Fig. 6 displays the results of the stability test in terms of the evolution of the mass activity with the extended cycling treatment for mass-selected Pt_xGd nanoparticles with average particle size of 5 nm, 8 nm, and 9 nm. For comparison purpose, the stability test results obtained with the most active Pt_xY catalyst (9 nm), as well as the initial activity of Pt 3-nm nanoparticles, are included in Fig. 6. It can be seen that for the three analyzed sizes the magnitude of the ORR activity losses is similar to that found with the Pt_xY nanoparticles, that is 30–55% [70], and that most of the activity loss occurs in the early stages of the stability test (first 1000 cycles). According to the CO-stripping analysis data, the electrochemical active surface area remains invariable after the stability test, indicating that a possible decrease of the available surface area (e.g. nanoparticles sintering, agglomeration, or detachment) cannot be accounted for the ORR activity losses. A similar conclusion could be extracted from the results of the IL-TEM analysis, shown in Fig. 4 for the case of the Pt_xGd 8-nm catalyst. As seen, no significant changes were detected in the catalyst general morphology after the stability test, with the exception of the dissolution of the oxide layer covering the as-prepared nanoparticles. The most active Pt_xGd nanoparticles (8 nm) retain 70% of the initial activity after 10,000 cycles, indicating that their stability is comparable (or slightly better) than that of Pt_xY nanoparticles of the optimum size (9 nm) [70]. Consequently, even after the extended potential cycling treatment, the Pt_xGd nanoparticles of 8 nm are still ~5 times more active than pure Pt nanoparticles with a comparable size and ~2.8 times more active than the maximum mass activity achieved with the mass-selected Pt nanoparticles (3 nm).

3.5. EXAFS analysis of Pt_xGd catalysts

Motivated by our previous investigation on polycrystalline Pt_5Gd, which revealed that the compressive strain was the main

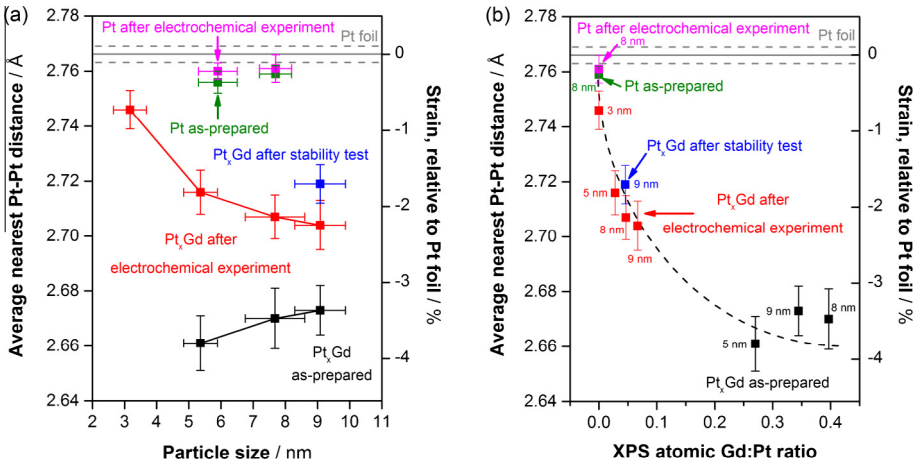

Fig. 7. (a) Average nearest-neighbor Pt–Pt distance measured by EXAFS as a function of the particle size for Pt$_x$Gd nanoparticles as-prepared (black), after electrochemical experiment (red) and after stability test (blue). For comparison purpose, the EXAFS results obtained for as-prepared (green) and electrochemically tested (pink) mass-selected Pt nanoparticles, reported in our preceding publication [70], are also shown; (b) average nearest-neighbor Pt–Pt distance measured by EXAFS as a function of the atomic Gd:Pt ratio estimated from XPS measurements for Pt$_x$Gd nanoparticles as-prepared (black), after electrochemical experiment (red) and after stability test (blue). The Pt–Pt interatomic distances determined by EXAFS in our previous work for as-prepared (green) and electrochemically tested (pink) mass-selected Pt nanoparticles, with zero Gd content, are shown for comparison [70]. The corresponding average particle size is specified. Measurements were performed in situ on a Pt foil (continuous gray horizontal line in a and b; the dashed gray horizontal lines show the error from the fitting software, see details in the Supporting information) as a reference. The left *y*-axis in (a and b) represents the nearest-neighbor Pt–Pt distance, whereas the right *y*-axis shows the strain percentage relative to the Pt–Pt distance measured for the Pt foil. The horizontal error bars in (a) account for the standard deviation in the particle size distribution (PSD) and the vertical error bars in (a and b) represent the standard deviation from the fitting software, respectively. The dashed black line in (b) serves as a guide for the eye. (For interpretation of the references to color in this figure legend, the reader is referred to the web version of this article.)

cause of the superior of performance of the alloy compared to pure Pt [60], we carried out grazing-incident extended X-ray absorption fine structure measurements (GI-EXAFS) for the quantification of the strain in the Pt$_x$Gd nanoparticles. For that purpose, samples as-prepared, after the standard electrochemical experiment and after the long-term stability test, were considered. The average nearest-neighbor distances between the Pt atoms were calculated through fitting of the EXAFS spectra. Details of the fitting procedure are described in detail in the Supplementary information. The result of the analysis is summarized in Fig. 7(a), where the Pt–Pt interatomic distance and the consequent compressive strain are plotted versus the average nanoparticle size for the three different experimental conditions. The EXAFS results obtained for as-prepared and electrochemically tested mass-selected Pt nanoparticles, reported in our preceding publication [70], are also presented. The average Pt–Pt distance for bulk Pt (Pt foil) is included in the plot for comparison and used for the estimation of the relative strain. In general, the as-prepared Pt$_x$Gd nanoparticles exhibit a smaller Pt–Pt distance than bulk Pt, indicating the existence of a compressive strain before the electrochemical analysis. The magnitude of such strain slightly decreases with the nanoparticle size, changing from −3.8% to −3.4% (compared to bulk Pt) for the 5-nm and the 9-nm nanoparticles, respectively. In the case of the catalysts after ORR test, they show significant larger Pt–Pt distances compared to the as-prepared samples but still lower compared to bulk Pt. The Pt–Pt distances after the standard electrochemical test are remarkably size dependent, varying smoothly from −0.7% to −2.2% for the 3 nm and the 9 nm size catalysts, respectively. In addition, the 9-nm Pt$_x$Gd sample subjected to the stability test exhibits less compressive strain than the counterpart after the conventional electrochemical measurement (−1.7% versus −2.2%, respectively), demonstrating that the accelerated stability test produces some relaxation in the Pt$_x$Gd nanoparticles. On the other hand, the average Pt–Pt distance/strain estimated by EXAFS measurements can be also associated with the XPS atomic Gd:Pt ratio of the Pt$_x$Gd nanoparticles under different conditions, being the corresponding relationship displayed in Fig. 7(b) (the data for mass-selected Pt nanoparticles and Pt foil presented for comparative purpose). The obtained trend reveals that the compressive strain in the Pt$_x$Gd nanoparticles is strongly related to the Gd content in the catalyst, increasing with the fraction of solute atoms.

4. Discussion

The interpretation of the XPS spectra shown in Fig. 2 combined with the angle-resolved XPS results of polycrystalline Pt$_5$Gd from our previous research (see Section 1) [60] strongly supports the formation of a core/shell structure after acid leaching of Gd atoms from the outermost layers of the nanoparticles. Therefore, such model can be also used for explaining the trends derived from the EXAFS analysis, shown in Fig. 7. We could rationalize the obtained findings considering that the as-prepared Pt$_x$Gd nanoparticles are under compressive strain as a result of the alloying; this is to be expected, given that the closest nearest-neighbor Pt–Pt distance in Pt$_5$Gd hexagonal structure is 2.65 Å, or ∼5% compressive strain relative to pure Pt (2.77 Å) [60,90] (see Fig. S1 in the Supplementary information). Once the Pt$_x$Gd nanoparticles are exposed to the electrolyte and subjected to the electrochemical characterization, the Gd atoms are leached out from the outermost atomic layers of the nanoparticles, leading to the formation of a pure Pt overlayer; this overlayer would be under compressive strain, induced by the underlying Pt$_x$Gd alloy core, resembling the structure of polycrystalline Pt$_5$Gd after electrochemical characterization [60]. Similarly, the scanning transmission electron microscopy energy-dispersive X-ray spectroscopy (STEM-EDS) mapping of mass-selected Pt$_x$Y nanoparticles revealed that a core/shell structure was developed after the ORR test, the Pt-rich being shell ∼1 nm thick, in agreement with the thickness of ∼3 monoatomic layers estimated for polycrystalline Pt–lanthanides alloys [70]. Logically, some strain relief could occur in the pure Pt shell of the Pt$_x$Gd nanoparticles in the absence of the Gd atoms. However, previous investigations with single crystal surfaces have revealed that some degree of compression would still be retained in the

outermost surface of the layer Pt shell [39]. Additionally, the size dependence for the strain after the ORR presented in Fig. 7(a) is due to the smaller pure alloy core for smaller nanoparticles, as also evidenced by the size dependence of Gd:Pt ratio in Fig. 7(b).

It is interesting to note that the strain in the 9-nm nanoparticles relaxes further, following the stability test. To some degree, this is only to be accepted; once the Gd is removed from the overlayer, there will be a driving force for it to relax toward pure Pt. It is curious, however, to note that in the case of the 9-nm particle, this relaxation is accompanied by a slight increase in the Pt:Gd XPS ratio, as shown in Fig. 7(b); this is analogous to the behavior of extended surfaces of polycrystalline Pt_5La and Pt_5Ce alloys following extended cycling [59]. Since Gd diffusion is likely to be very slow at room temperature through the Pt overlayer (see Section 1), we speculate that the dealloying occurs via an alternative mechanism, perhaps involving subsurface oxide formation [91]. Nonetheless, the majority of the activity losses occur during the first 1000 cycles, as shown in Fig. 6. This suggests that the rate of degradation slows significantly after 1000 cycles, at which point the catalyst has reached some kind of metastable state.

In order to gain some insight into the role of the strain in the ORR activity of the Pt_xGd nanoparticles, the specific activity is plotted as a function of the corresponding strain relative to Pt foil after ORR and after stability test in Fig. 8. In addition, the previous results of activity versus strain after ORR for Pt_xY NPs and for Pt NPs are included for comparison. *As a result, it is manifest that the ORR activity of Pt, Pt_xY, and Pt_xGd all follows the same trend, that is the activity enhancement is largely controlled by the strain in the nanoparticles*. This is also consistent with Strasser and co-workers' investigations of dealloyed Pt_xCu nanoparticles [39]. It should be noted that the strain dependence of the ORR activity reported in Ref. [39] was found significantly less intense than that presented in this work, most likely due to excessive relaxation of the compressive strain in the Pt overlayer of the dealloyed Pt_xCu nanoparticles [39]. Moreover, the trend displayed in Fig. 8 also resembles the relationship established in our previous work focused on polycrystalline Pt–lanthanides alloys [59], where the specific activity of polycrystalline Pt_5Gd, Pt_5Ce, and Pt_5La was correlated with the interatomic Pt distance in the bulk, based on X-ray diffraction (XRD) measurements. Consequently, we conjecture that the compressive strain causes the weakening of the oxygenated intermediates adsorption, leading to the consequent enhancement of the ORR activity. According to DFT calculations, the necessary strain for optimizing the ORR performance is −2% (relative to an unstrained Pt(1 1 1) surface) [39]. This value is reached by the bulk compressive strain of the most active Pt_xGd nanoparticles (−2.2%), without reaching a maximum in activity. We expect that the local strain within the outermost layer of the Pt shell, which is responsible for the ORR activity, would be somewhat reduced compared to the overall strain plotted in Fig. 8, because of strain relaxation. This would result in an unknown shift of the plot to the right and, subsequently, we propose that the trend exhibited in Fig. 8 represents *the strong *OH binding side of a volcano plot. Accordingly, should a slightly greater degree of strain be imposed onto the surface*, by refining the atomic ratio of the second metal or increasing the nanoparticle size, *it might be possible to reach the peak of the volcano*.

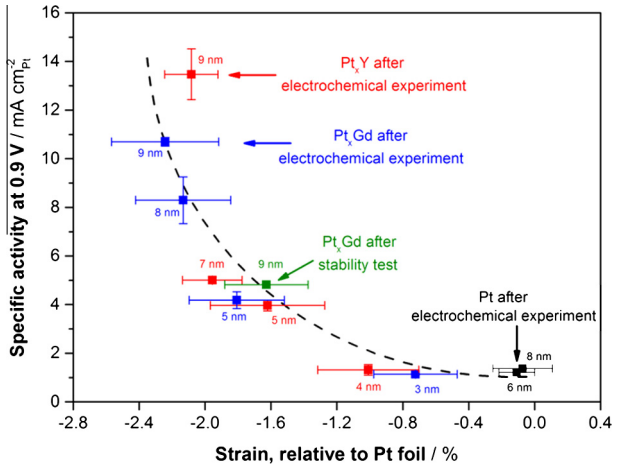

Fig. 8. Specific activity results for the ORR on Pt_xGd nanoparticles as a function of the strain, relative to bulk Pt, determined through EXAFS after electrochemical experiment (blue) and after the stability test (green). Data collected from Fig. 5, Fig. 6, and Fig. 7. The previous data reported for mass-selected Pt_xY (red) and Pt nanoparticles (black) after electrochemical experiment are included for comparison purposes [70]. The dashed black line acts as a guide for the eye. The horizontal and vertical error bars show the standard deviation in the strain estimation and in the electrochemical measurements, respectively. (For interpretation of the references to color in this figure legend, the reader is referred to the web version of this article.)

5. Conclusions

We have shown in the present work that the excellent catalytic properties of polycrystalline Pt_5Gd (enhanced ORR activity compared to pure Pt and stability upon cycling) also extend to nanoparticles. The maximum mass activity reached with the Pt_xGd nanoparticles (8 nm, 3.6 A (mg Pt)$^{-1}$ at 0.9 V) represents a notable improvement compared to our preceding results obtained with Pt_xY nanoparticles; in the literature, it is only surpassed by Pt_3Ni nanoframes [41]. Additionally, the optimum Pt_xGd catalyst exhibits similar, albeit very slightly improved, stability versus the most active Pt_xY nanoparticles previously reported (70% retention of the initial activity versus 63% for Pt_xY).

In addition, we have also confirmed that the mechanism for the ORR enhancement accounts for the compressive strain within the Pt shell induced by the Pt_xGd core. As a result, a direct relationship between the ORR activity of the Pt_xGd nanoparticles and their compressive strain can be established. We have also shown that the activity of pure Pt nanoparticles, Pt_xY, and Pt_xGd can all be correlated to the lattice strain.

Our work confirms that Pt_xGd alloy nanoparticles are of great interest for applications in PEMFC cathodes. Nevertheless, we are aware that the ultrahigh vacuum procedure used in this research is not valid for catalyst mass production; eventually low-priced chemical methods should be employed for such purpose. Therefore, our efforts are currently directed to the development of suitable chemical procedures to obtain Pt_xGd alloy in nanoparticulate form; using such methods we may have control over both particle size and Gd content, and ultimately the strain, which controls the oxygen reduction activity.

Acknowledgments

We thankfully acknowledge the EU PF7's initiative Fuel Cell and Hydrogen Joint Undertaking's project CathCat (GA 303492), the Danish National Research Foundation's Center for Individual Nanoparticle Functionality (DNRF54), and the Danish Ministry of Science's UNIK initiative Catalysis for Sustainable Energy (CASE) for providing the funding for this research. We also thank the Danish Council for Strategic Research's project NACORR. The A.P. Møller and Chastine Mc-Kinney Møller Foundation is gratefully acknowledged for its contribution toward the establishment of the Centre for Electron Nanoscopy in the Technical University of Denmark. This research was partly carried out at the Stanford Synchrotron Radiation Lightsource, a National User Facility operated by

Stanford University on behalf of the U.S. Department of Energy, Office of Basic Energy Sciences. We thank John R. Bargar, Apurva Mehta, Ryan C. Davis, Matthew Latimer, and Erik J. Nelson for their support with the GI-EXAFS setup and helpful discussions.

Appendix A. Supplementary material

Supplementary data associated with this article can be found, in the online version, at http://dx.doi.org/10.1016/j.jcat.2014.12.012.

References

[1] A. Wieckowski, M. Neurock, Adv. Phys. Chem. 2011 (2011) 1.
[2] J.K. Nørskov, T. Bligaard, J. Rossmeisl, C.H. Christensen, Nat. Chem. 1 (2009) 37.
[3] P. Sabatier, Ber. Dtsch. Chem. Ges. 44 (1911) 1984.
[4] J.K. Nørskov, J. Rossmeisl, A. Logadottir, L. Lindqvist, J.R. Kitchin, T. Bligaard, H. Jónsson, J. Phys. Chem. B 108 (2004) 17886.
[5] J. Rossmeisl, A. Logadottir, J.K. Nørskov, Chem. Phys. 319 (2005) 178.
[6] J. Greeley, T.F. Jaramillo, J. Bonde, I.B. Chorkendorff, J.K. Nørskov, Nat. Mater. 5 (2006) 909.
[7] J.K. Nørskov, T. Bligaard, A. Logadottir, J.R. Kitchin, J.G. Chen, S. Pandelov, U. Stimming, J. Electrochem. Soc. 152 (2005) J23.
[8] A.A. Peterson, J.K. Nørskov, J. Phys. Chem. Lett. 3 (2012) 251.
[9] H.A. Hansen, I.C. Man, F. Studt, F. Abild-Pedersen, T. Bligaard, J. Rossmeisl, Phys. Chem. Chem. Phys. 12 (2010) 283.
[10] I.C. Man, H.Y. Su, F. Calle-Vallejo, H.A. Hansen, J.I. Martínez, N.G. Inoglu, J. Kitchin, T.F. Jaramillo, J.K. Nørskov, J. Rossmeisl, Chem. Cat. Chem. 3 (2011) 1159.
[11] H. Dau, C. Limberg, T. Reier, M. Risch, S. Roggan, P. Strasser, Chem. Cat. Chem. 2 (2010) 724.
[12] M.T.M. Koper, J. Electroanal. Chem. 660 (2011) 254.
[13] S. Siahrostami, A. Verdaguer-Casadevall, M. Karamad, D. Deiana, P. Malacrida, B. Wickman, M. Escudero-Escribano, E.A. Paoli, R. Frydendal, T.W. Hansen, I. Chorkendorff, I.E.L. Stephens, J. Rossmeisl, Nat. Mater. 12 (2013) 1137.
[14] T.F. Jaramillo, K.P. Jørgensen, J. Bonde, J.H. Nielsen, S. Horch, I. Chorkendorff, Science 317 (2007) 100.
[15] A.A. Peterson, F. Abild-Pedersen, F. Studt, J. Rossmeisl, J.K. Nørskov, Energy Environ. Sci. 3 (2010) 1311.
[16] V. Stamenkovic, B.S. Mun, K.J.J. Mayrhofer, P.N. Ross, N.M. Markovic, J. Rossmeisl, J. Greeley, J.K. Nørskov, Angew. Chem. Int. Ed. 45 (2006) 2897.
[17] A.U. Nilekar, M. Mavrikakis, Surf. Sci. 602 (2008) L89.
[18] J. Greeley, I.E.L. Stephens, A.S. Bondarenko, T.P. Johansson, H.A. Hansen, T.F. Jaramillo, J. Rossmeisl, I. Chorkendorff, J.K. Nørskov, Nat. Chem. 1 (2009) 552.
[19] I.E.L. Stephens, A.S. Bondarenko, F.J. Perez-Alonso, F. Calle-Vallejo, L. Bech, T.P. Johansson, A.K. Jepsen, R. Frydendal, B.P. Knudsen, J. Rossmeisl, I. Chorkendorff, J. Am. Chem. Soc. 133 (2011) 5485.
[20] V. Viswanathan, H.A. Hansen, J. Rossmeisl, J.K. Nørskov, J. Phys. Chem. Lett. 3 (2012) 2948.
[21] A. Verdaguer-Casadevall, D. Deiana, M. Karamad, S. Siahrostami, P. Malacrida, T.W. Hansen, J. Rossmeisl, I. Chorkendorff, I.E.L. Stephens, Nano Lett. 14 (2014) 1603.
[22] A.S. Bandarenka, H.A. Hansen, J. Rossmeisl, I.E.L. Stephens, Phys. Chem. Chem. Phys. 16 (2014) 13625.
[23] H.A. Gasteiger, S.S. Kocha, B. Sompalli, F.T. Wagner, Appl. Catal. B: Environ. 56 (2005) 9.
[24] K.C. Neyerlin, W. Gu, J. Jorne, H.A. Gasteiger, J. Electrochem. Soc. 154 (2007) B631.
[25] K.E. Swider-Lyons, S.A. Campbell, J. Phys. Chem. Lett. 4 (2013) 393.
[26] C.M. Zalitis, D. Kramer, A.R. Kucernak, Phys. Chem. Chem. Phys. 15 (2013) 4329.
[27] M. Wesselmark, B. Wickman, C. Lagergren, G. Lindbergh, Electrochem. Commun. 12 (2010) 1585.
[28] F.T. Wagner, B. Lakshmanan, M.F. Mathias, J. Phys. Chem. Lett. 1 (2010) 2204.
[29] A. Rabis, P. Rodriguez, T.J. Schmidt, ACS Catal. 2 (2012) 864.
[30] I.E.L. Stephens, A.S. Bondarenko, U. Grønbjerg, J. Rossmeisl, I. Chorkendorff, Energy Environ. Sci. 5 (2012) 6744.
[31] A.S. Bondarenko, I.E.L. Stephens, H.A. Hansen, F.J. Pérez-Alonso, V. Tripkovic, T.P. Johansson, J. Rossmeisl, J.K. Nørskov, I. Chorkendorff, Langmuir 27 (2011) 2058.
[32] D. Friebel, V. Viswanathan, D.J. Miller, T. Anniyev, H. Ogasawara, A.H. Larsen, C.P. O'Grady, J.K. Nørskov, A. Nilsson, J. Am. Chem. Soc. 134 (2012) 9664.
[33] V. Viswanathan, H.A. Hansen, J. Rossmeisl, J.K. Nørskov, ACS Catal. 2 (2012) 1654.
[34] H.S. Casalongue, S. Kaya, V. Viswanathan, D.J. Miller, D. Friebel, H.A. Hansen, J.K. Nørskov, A. Nilsson, H. Ogasawara, Nat. Commun. 4 (2013) 2817.
[35] J. Rosmeisl, G.S. Karlberg, T. Jaramillo, J.K. Nørskov, Faraday Discuss. 140 (2008) 337.
[36] J.R. Kitchin, J.K. Nørskov, M.A. Barteau, J.G. Chen, J. Chem. Phys. 120 (2004) 10240.
[37] F. Calle-Vallejo, J.I. Martínez, J.M. García-Lastra, J. Rossmeisl, M.T.M. Koper, Phys. Rev. Lett. 108 (2012) 116103.
[38] M. Mavrikakis, B. Hammer, J. Nørskov, Phys. Rev. Lett. 81 (1998) 2819.
[39] P. Strasser, S. Koh, T. Anniyev, J. Greeley, K. More, C. Yu, Z. Liu, S. Kaya, D. Nordlund, H. Ogasawara, M.F. Toney, A. Nilsson, Nat. Chem. 2 (2010) 454.
[40] S. Mukerjee, S. Srinivasan, M.P. Soriaga, J. McBreen, J. Electrochem. Soc. 142 (1995) 1409.
[41] C. Chen, Y. Kang, Z. Huo, Z. Zhu, W. Huang, H.L. Xin, J.D. Snyder, D. Li, J.A. Herron, M. Mavrikakis, M. Chi, K.L. More, Y. Li, N.M. Markovic, G.A. Somorjai, P. Yang, V.R. Stamenkovic, Science 343 (2014) 1339.
[42] S. Chen, P.J. Ferreira, W. Sheng, N. Yabuuchi, L.F. Allard, Y. Shao-Horn, J. Am. Chem. Soc. 130 (2008) 13818.
[43] S.I. Choi, S. Xie, M. Shao, J.H. Odell, N. Lu, H.C. Peng, L. Protsailo, S. Guerrero, J. Park, X. Xia, J. Wang, M.J. Kim, Y. Xia, Nano Lett. 13 (2013) 3420.
[44] L. Gan, M. Heggen, S. Rudi, P. Strasser, Nano Lett. 12 (2012) 5423.
[45] I. Spanos, J.J.K. Kirkensgaard, K. Mortensen, M. Arenz, J. Power Sources 245 (2014) 908.
[46] V.R. Stamenkovic, B.S. Mun, K.J.J. Mayrhofer, P.N. Ross, N.M. Markovic, J. Am. Chem. Soc. 128 (2006) 8813.
[47] T. Wadayama, N. Todoroki, Y. Yamada, T. Sugawara, K. Miyamoto, Y. Iijama, Electrochem. Commun. 12 (2010) 1112.
[48] N. Todoroki, Y. Iijima, R. Takahashi, Y. Asakimori, T. Wadayama, J. Electrochem. Soc. 160 (2013) F591.
[49] C. Wang, M. Chi, D. Li, D. Strmcnik, D. van der Vliet, G. Wang, V. Komanicky, K.C. Chang, A.P. Paulikas, D. Tripkovic, J. Pearson, K.L. More, N.M. Markovic, V.R. Stamenkovic, J. Am. Chem. Soc. 133 (2011) 14396.
[50] V.R. Stamenkovic, B. Fowler, B.S. Mun, G. Wang, P.N. Ross, C.A. Lucas, N.M. Markovic, Science 315 (2007) 493.
[51] T. Toda, H. Igarashi, H. Uchida, M. Watanabe, J. Electrochem. Soc. 146 (1999) 3750.
[52] M. Watanabe, K. Tsurumi, T. Mizukami, T. Nakamura, P. Stonehart, J. Electrochem. Soc. 141 (1994) 2659.
[53] A. Ohma, K. Shinohara, A. Iiyama, T. Yoshida, A. Daimaru, ECS Trans. 41 (2011) 775.
[54] H.L. Xin, J.A. Mundy, Z. Liu, R. Cabezas, R. Hovden, L.F. Kourkoutis, J. Zhang, N.P. Subramanian, R. Makharia, F.T. Wagner, D.A. Muller, Nano Lett. 12 (2012) 490.
[55] The US Department of Energy (DOE), Energy Efficiency and Renewable Energy, http://www.eere.energy.gov/hydrogenandfuelcells/mypp/pdfs/fuel_cells.pdf; and the US DRIVE Fuel Cell Technical Team Technology Roadmap, http://www.uscar.org/guest/teams/17/Fuel-Cell-Tech-Team, 2013.
[56] S. Chen, H.A. Gasteiger, K. Hayakawa, T. Tada, Y. Shao-Horn, J. Electrochem. Soc. 157 (2010) A82.
[57] K.C. Neyerlin, R. Srivastava, C. Yu, P. Strasser, J. Power Sources 186 (2009) 261.
[58] L. Dubau, M. López-Haro, L. Castanheira, J. Durst, M. Chatenet, P. Bayle-Guillemaud, L. Guétaz, N. Caqué, E. Rossinot, F. Maillard, Appl. Catal. B: Environ. 142–143 (2013) 801.
[59] P. Malacrida, M. Escudero-Escribano, A. Verdaguer-Casadevall, I.E.L. Stephens, I. Chorkendorff, J. Mater. Chem. A 2 (2014) 4234.
[60] M. Escudero-Escribano, A. Verdaguer-Casadevall, P. Malacrida, U. Grønbjerg, B.P. Knudsen, A.K. Jepsen, J. Rossmeisl, I.E.L. Stephens, I. Chorkendorff, J. Am. Chem. Soc. 134 (2012) 16476.
[61] P.C.K. Vesborg, T.F. Jaramillo, RSC Adv. 2 (2012) 7933.
[62] N. Schumacher, K. Andersson, L.C. Grabow, M. Mavrikakis, J. Nerlov, I. Chorkendorff, Surf. Sci. 602 (2008) 702.
[63] T.P. Johansson, E.T. Ulrikkeholm, P. Hernández-Fernández, M. Escudero-Escribano, P. Malacrida, I.E.L. Stephens, I. Chorkendorff, Phys. Chem. Chem. Phys. 16 (2014) 13718.
[64] C.A. Menning, J.G. Chen, Top. Catal. 53 (2010) 338.
[65] I.E.L. Stephens, A.S. Bondarenko, L. Bech, I. Chorkendorff, Chem. Cat. Chem. 4 (2012) 341.
[66] S.J. Yoo, S.K. Kim, T.Y. Jeon, S.J. Hwang, J.G. Lee, S.C. Lee, K.S. Lee, Y.H. Cho, Y.E. Sung, T.H. Lim, Chem. Commun. 47 (2011) 11414.
[67] B. Cordero, V. Gómez, A.E. Platero-Prats, M. Revés, J. Echeverría, E. Cremades, F. Barragán, S. Alvarez, Dalton Trans. (2008) 2832.
[68] M. Pourbaix, Atlas of Electrochemical Equilibria in Aqueous Solutions, Pergamon Press, Bristol, 1966. p. 330.
[69] Y. Luo, A. Habrioux, L. Calvillo, G. Granozzi, N. Alonso-Vante, Chem. Phys. Chem. 15 (2014) 2136.
[70] P. Hernández-Fernández, F. Masini, D.N. McCarthy, C.E. Strebel, D. Friebel, D. Deiana, P. Malacrida, A. Nierhoff, A. Bodin, A.M. Wise, J.H. Nielsen, T.W. Hansen, A. Nilsson, I.E.L. Stephens, I. Chorkendorff, Nat. Chem. 6 (2014) 732.
[71] F.J. Pérez-Alonso, D.N. McCarthy, A. Nierhoff, P. Hernández-Fernández, C. Strebel, I.E.L. Stephens, J.H. Nielsen, I. Chorkendorff, Angew. Chem. Int. Ed. 51 (2012) 4641.
[72] D.N. McCarthy, C.E. Strebel, T.P. Johansson, A. den Dunnen, J.H. Nielsen, I. Chorkendorff, J. Phys. Chem. C 116 (2012) 15353.
[73] M. Nesselberger, M. Roefzaad, R.F. Hamou, P.U. Biedermann, F.F. Schweinberger, S. Kunz, K. Schloegl, G.K.H. Wiberg, S. Ashton, U. Heiz, K.J.J. Mayrhofer, M. Arenz, Nat. Mater. 12 (2013) 919.
[74] F. Yin, Z.W. Wang, R.E. Palmer, J. Am. Chem. Soc. 133 (2011) 10325.
[75] F. Masini, C.E. Strebel, D.N. McCarthy, A.U.F. Nierhoff, J. Kehres, E.M. Fiordaliso, J.H. Nielsen, I. Chorkendorff, J. Catal. 308 (2013) 282.
[76] C. Galeano, J.C. Meier, V. Peinecke, H. Bongard, I. Katsounaros, A.A. Topalov, A. Lu, K.J.J. Mayrhofer, F. Schüth, J. Am. Chem. Soc. 134 (2012) 20457.
[77] Z.Y. Li, J.P. Wilcoxon, F. Yin, Y. Chen, R.E. Palmer, R.L. Johnston, Faraday Discuss. 138 (2008) 363.

[78] J. Speder, L. Altmann, M. Bäumer, J.J.K. Kirkensgaard, K. Mortensen, M. Arenz, RSC Adv. 4 (2014) 14971.
[79] A. Zana, J. Speder, N.E.A. Reeler, T. Vosch, M. Arenz, Electrochim. Acta 114 (2013) 455.
[80] R.A. Martínez-Rodríguez, F.J. Vidal-Iglesias, J. Solla-Gullón, C.R. Cabrera, J.M. Feliu, J. Am. Chem. Soc. 136 (2014) 1280.
[81] F. Masini, P. Hernández-Fernández, D. Deiana, C.E. Strebel, D.N. McCarthy, A. Bodin, P. Malacrida, I. Stephens, I. Chorkendorf, Phys. Chem. Chem. Phys. (2014), http://dx.doi.org/10.1039/C4CP02144D.
[82] H. Haberland, M. Karrais, M. Mall, Y. Thurner, J. Vac. Sci. Technol. A 10 (1992) 3266.
[83] B. von Issendorff, R.E. Palmer, Rev. Sci. Instrum. 70 (1999) 4497.
[84] C.D. Wagner, L.E. Davis, M.V. Zeller, J.A. Taylor, R.H. Raymond, L.H. Gale, Surf. Interface Anal. 3 (1981) 211.
[85] S. Tanuma, C.J. Powell, D.R. Penn, Surf. Interface Anal. 17 (1991) 911.
[86] F.J. Perez-Alonso, C.F. Elkjær, S.S. Shim, B.L. Abrams, I.E.L. Stephens, I. Chorkendorff, J. Power Sources 196 (2011) 6085.
[87] F. Maillard, E.R. Savinova, U. Stimming, J. Electroanal. Chem. 599 (2007) 221.
[88] D. Raiser, J.P. Deville, J. Electron Spectrosc. Relat. Phenomena. 57 (1991) 91.
[89] M. Nesselberger, S. Ashton, J.C. Meier, I. Katsounaros, K.J.J. Mayrhofer, M. Arenz, J. Am. Chem. Soc. 133 (2011) 17428.
[90] W. Bronger, J. Less Common Metals 12 (1967) 63.
[91] D. Friebel, D.J. Miller, C.P. O'Grady, T. Anniyev, J. Bargar, U. Bergmann, H. Ogasawara, K.T. Wikfeldt, L.G.M. Pettersson, A. Nilsson, Phys. Chem. Chem. Phys. 13 (2011) 262.